Journal of Manufacturing Processes 127 (2024) 698–708

Contents lists available at ScienceDirect

Journal of Manufacturing Processes

journal homepage: www.elsevier.com/locate/manpro

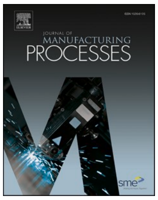

Relationship between the superelasticity and strain field around Ni_4Ti_3 nano-precipitates in NiTi shape memory alloy via laser powder bed fusion

Y. Yang [a], Y.Q. Zhang [a], H.Z. Lu [a,b,*], Y. Luo [a], T.H. Long [a], W.T. Tong [c], Y. Zhang [c], X. Yu [d], C. Yang [a,*]

[a] National Engineering Research Center of Near-net-shape Forming for Metallic Materials, Guangdong Provincial Key Laboratory for Processing and Forming of Advanced Metallic Materials, South China University of Technology, Guangzhou 510640, China
[b] School of Mechatronic Engineering, Guangdong Polytechnic Normal University, Guangzhou 510665, China
[c] Guizhou Yong Hong Aviation Machinery Co. Ltd, Guizhou 550009, China
[d] Shenyang Aeroengine Research Institute, Aero Engine Corporation of China, Shenyang 110015, China

ARTICLE INFO

Keywords:
NiTi
Laser powder bed fusion
Precipitates
Superelasticity

ABSTRACT

Although the simulation results had demonstrated that the strain field introduced by Ni_4Ti_3 nano-precipitates in NiTi shape memory alloys (SMAs) was related with their superelasticity inherently, the corresponding experimental result was rarely documented heretofore, especially in additive manufactured NiTi SMAs. In this work, we tailor the morphologies and resultant strain field of Ni_4Ti_3 nano-precipitates by heat treatment of a NiTi SMA subjected to laser powder bed fusion (LPBF), and further authenticate relationship between the superelasticity and the strain field in the LPBF NiTi samples. When holding times were 1 h, 3 h, and 5 h at aging temperature of 350 °C after solution treatment, the Ni_4Ti_3 nano-precipitates in the LPBF NiTi samples exhibit spherical, ellipsoidal, and lenticular morphologies, respectively. Accordingly, the strain field around Ni_4Ti_3 nano-precipitates in B2 matrix decrease from 0.15 % to 0.13 % and 0.10 %, respectively. The LPBF and aged NiTi samples present large superelasticity, which exceeds 6 % recovery strain together with high recovery rate of >99 % during 10-times cyclic compression loading. Interestingly, the LPBF and aged sample with the spherical Ni_4Ti_3 and highest strain field displays the worst superelasticity stability, while the one with the lenticular Ni_4Ti_3 and smallest strain field exhibits the relatively stable and biggest superelasticity of 6.36 %. Basically, this is attributed to different mechanisms between the Ni_4Ti_3 nano-precipitates and dislocations generated during cyclic loading, which is induced by different interfaces between the Ni_4Ti_3 and B2 matrix in the three types of the NiTi samples. For the sample with the highest strain field, its spherical Ni_4Ti_3 was cut through by generated dislocations due to coherent interface between the spherical Ni_4Ti_3 and B2 matrix. In contrast, the one with the smallest strain field, its lenticular Ni_4Ti_3 can impede effectively generated dislocations because of semi-coherent or non-coherent interface between the lenticular Ni_4Ti_3 and B2 matrix. Therefore, these results can provide meaningful insights into tailoring the nano-precipitates and thereby obtaining excellent superelasticity of NiTi SMAs by LPBF.

1. Introduction

NiTi shape memory alloys (SMAs) are widely used in aerospace applications, surgical instruments, and medical devices because of their superelasticity, shape memory effect, good biocompatibility, and high corrosion resistance [1–3]. It has been confirmed that strain fields introduced by various precipitates play an important role in the modulation of functional properties for NiTi SMAs. Tirry et al. [4] found and confirmed that there were strain field surrounding the Ni_4Ti_3 precipitate in thermally treated NiTi SMAs by atomic-resolution transmission electron microscopy and geometrical phase analysis, which introduced by the matrix-precipitate lattice mismatch. Based on the potential reinforcement from the strain field, enhanced strength was obtained in the coarse-grained $Ni_{50.8}Ti_{49.2}$ SMA by Wang et al. [5]. They claimed that evenly-distributed Ni_4Ti_3 nano-precipitate and high-density dislocations could resist plastic deformation during the stress-induced martensite transformation, thereby improving the superelasticity stability of $Ni_{50.8}Ti_{49.2}$ SMA, and only 0.5 % irrecoverable strain was

---

* Corresponding authors.
E-mail addresses: hzlu@gpnu.edu.cn (H.Z. Lu), cyang@scut.edu.cn (C. Yang).

https://doi.org/10.1016/j.jmapro.2024.08.023
Received 10 October 2023; Received in revised form 26 June 2024; Accepted 12 August 2024
Available online 15 August 2024

observed after 20-times cyclic tension. Meanwhile, Yamamoto et al. [6], Tomozawa et al. [7], and Chang et al. [8] pointed out that the coherent strain field around the plate-like Guinier-Preston zones and the strain field around the nano-sized spherical semicoherent Ti_2Ni precipitates could result in the R phase transformation appearing in Ti-rich TiNi thin films. Furthermore, Ishida et al. [9] and Tadayyon et al. [10] found that microscale Ti_2Ni precipitate preferentially along grain boundaries, which had non-coherent relationship with matrix completely, caused fracture of NiTi SMAs at an early stage during plastic deformation, thus leading to a sharp decrease in ductility. It can be found that modulating and obtaining proper strain field in the matrix of NiTi SMAs can significantly improve their functional properties.

For the manufacturing process of NiTi SMAs, many researchers stressed that the manufacturing and machining process of NiTi are challenging owing to their low thermal conductivity, remarkable spring back effect, and high work hardening, which limits the applications of complex-shaped NiTi SMA parts [11–13]. As a commonly used additive manufacturing technology, laser powder bed fusion (LPBF) technique can fabricate NiTi parts from powder particles, which makes it available for complex NiTi SMA parts for biomedical implants [14–17]. However, during the LPBF process, the high heating and cooling rates (10^4–10^6 K/s [18,19]) of melt pools result in the existence of residual stress in the LPBF metallic parts [20,21], and complex thermal histories and local chemical compositional changes lead to the formation of unevenly-distributed precipitation phase in LPBF NiTi SMAs [22–25]. Undoubtedly, post-treatment processes are effective to weaken the adverse effects of above factors, and improve the mechanical and functional properties of LPBF NiTi SMAs. Recently, Li et al. [26] and Tan et al. [27] found that the microscale Ti_2Ni precipitate formed in LPBF $Ni_{44.3}Ti_{55.7}$ and $Ni_{45.2}Ti_{54.8}$ SMAs, and the mechanical properties of LPBF NiTi SMAs increased remarkably after heat treatment or hot isostatic press. Meanwhile, Lu et al. [28] pointed out that homogenization of Ti_2Ni nano-precipitate can be achieved by proper heat treatment in LPBF $Ni_{49.4}Ti_{50.6}$, and $Ni_{49.4}Ti_{50.6}$ with homogeneous globular Ti_2Ni nano-precipitate showed an excellent shape memory effect, with a recovery strain of 5.32 % and recovery rate of >98 % after ten loading-unloading cycles. However, the altered strain field around the Ti_2Ni nano-precipitate was ignored in above works. Furthermore, Cao et al. [29] obtained a compressive recovery strain of 4.6 % after ten loading-unloading cycles by introducing uniformly-distributed Ni_4Ti_3 nano-precipitate (50–200 nm) by heat treatment of $Ni_{51.4}Ti_{48.6}$ SMA. However, it should be noted that Cao et al. [29] did not investigate the microstructure evolution and relationship between the superelasticity and characteristics of Ni_4Ti_3 nano-precipitate thoroughly. Moreover, Saedi et al. [30,31] investigated the influence of heat treatment on the phase transformation behavior and compressive superelasticity for LPBF NiTi SMAs. However, the underlying mechanisms between altered microstructure and superelasticity had not been revealed systematically in these works. Therefore, systematic studies should be conducted on the evolution of precipitation phase during heat treatment, and relationship between precipitation phase and superelasticity should be established in LPBF NiTi SMAs [11,32].

In this study, different strain fields were introduced in the matrix of LPBF $Ni_{50.7}Ti_{49.3}$ SMA by tailoring the morphology of Ni_4Ti_3 nano-precipitate. Then, the phase transformation and superelasticity were studied in detail for LPBF $Ni_{50.7}Ti_{49.3}$. Moreover, the underlying mechanisms of varied microstructures and superelasticity in LPBF $Ni_{50.7}Ti_{49.3}$ with different strain fields were revealed in detail. The presented results in this study make it possible to obtain the desired superelasticity of LPBF NiTi SMAs via tailoring strain fields in their matrix.

2. Experimental

2.1. Material and LPBF

The as-received $Ni_{50.7}Ti_{49.3}$ powder was prepared by electrode induction-melting gas atomization technique. Fig. 1a shows most of NiTi powder had spherical or near-spherical shape. The size distribution in Fig. 1b demonstrates that the D_{50} of the NiTi powder was 33 μm. The XRD result in Fig. 1c shows single B2 austenite phase in the NiTi powder. The powder was implemented via an EOS M280 LPBF system in high-purity Ar atmosphere. Fig. 1d presents the processing strategy during LPBF. The rotation angle between adjacent layers was 67°, which was beneficial for the formability of LPBF $Ni_{50.7}Ti_{49.3}$ samples (Fig. 1d) [33]. The optimized LPBF parameters were 180 W laser power, 800 mm/s scanning speed, 30 μm layer thickness, and 80 μm hatch spacing [34]. Fig. 1e shows $Ni_{50.7}Ti_{49.3}$ samples having dimensions of $8.5 \times 6.5 \times 6.5$ mm^3 in x, y, z directions fabricated by LPBF. In particular, for the as-fabricated NiTi samples, heat treatment of solid solution at 950 °C for 5.5 h, followed by ice-water quenching, and aging treatment at 350 °C for 1 h, 3 h and 5 h, followed by ice-water quenching were conducted with high-purity Ar protection, which was aimed at tailoring the morphologies of Ni_4Ti_3 precipitate. Compression samples with 3 mm diameter and 6 mm length were produced by wire-electrode cutting for compressive test (Fig. 1f).

2.2. Characterization and test

The phases were identified using X-ray diffraction (XRD) analysis, specifically with Cu Kα radiation, conducted at room temperature (25 °C) using a D/MAX-2500/PC instrument. Differential scanning calorimetry (DSC) was employed to investigate phase transformation temperatures (TTs) with a cooling/heating rate of 10 °C/min, following the ASTM F2004–05 standard. The LPBF NiTi samples were polished and etched with a solution comprising 50 vol% H_2O, 40 vol% HNO_3, and 10 vol% HF. Subsequently, optical microscopy (OM) using a Leica DM 15000 M microscope and scanning electron microscopy (SEM) with a Philips XL-30 FEG instrument were utilized to analyze and reveal the microstructure of the NiTi samples. Electron backscattered diffraction (EBSD) analysis was measured using SEM at a step size of 1.4 μm and an operating voltage of 20 kV, and the measured EBSD data were post-processed using TSL OIM Analysis 7 software. Transmission electron microscopy (TEM) was conducted using a field emission gun high-resolution TEM (JEM-2100) with an acceleration voltage of 200 kV. TEM samples were prepared through twin-jet electro-polishing within a solution consisting of 4 vol% $HClO_4$ acid and 96 vol% C_2H_5OH at −30 °C, followed by ion-beam thinning using a Gatan 691 system. For evaluating the superelasticity, cylindrical samples were subjected to stress-controlled cyclic compressive loading using an INSTRON 8862 test platform. A constant strain rate of 5×10^{-4} s^{-1} was applied during both loading and unloading phases. Prior to the compressive test, all LPBF NiTi samples were heated to a temperature 10 °C above the austenite transformation finish temperature (A_f) and held for 5 min to ensure temperature uniformity.

3. Results

3.1. Phase transformation behaviors

Fig. 2 shows XRD results of the LPBF $Ni_{50.7}Ti_{49.3}$ samples. It is found that B2 austenite phase dominated in as-fabricated and solution NiTi samples, and the Miller indices (11−2) and (300) of R phase occurred in NiTi samples after aging treatment, which indicated that R phase formed in aged NiTi samples [35]. Besides, weak diffraction peaks of B19′ martensite in all NiTi samples demonstrated the existence of minor B19′ martensite in all LPBF NiTi samples. Meanwhile, weak diffraction peaks corresponding to the Ni_4Ti_3 phase in aged NiTi samples showed that the Ni_4Ti_3 phase might precipitate in the B2 austenite matrix after solution and aging treatment of the LPBF $Ni_{50.7}Ti_{49.3}$ samples [36].

Fig. 3a exhibits the DSC curves of LPBF NiTi samples under different states. The martensite start temperature (M_s), martensite finish temperature (M_f), austenite start temperature (A_s), and austenite finish

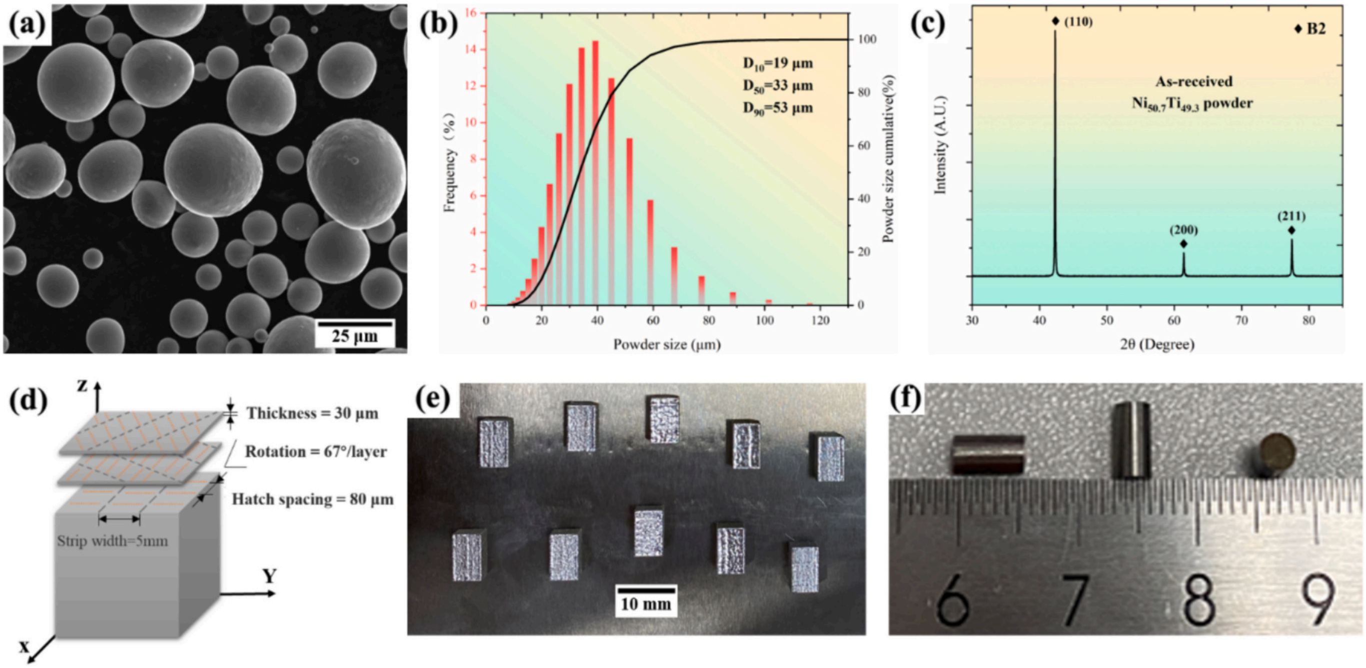

Fig. 1. (a) Morphology, (b) Size distribution, (c) X-ray diffraction pattern of NiTi powder, (d) Scanning path, (e) Fabricated NiTi samples, (f) Cylindrical LPBF NiTi samples for compressive test.

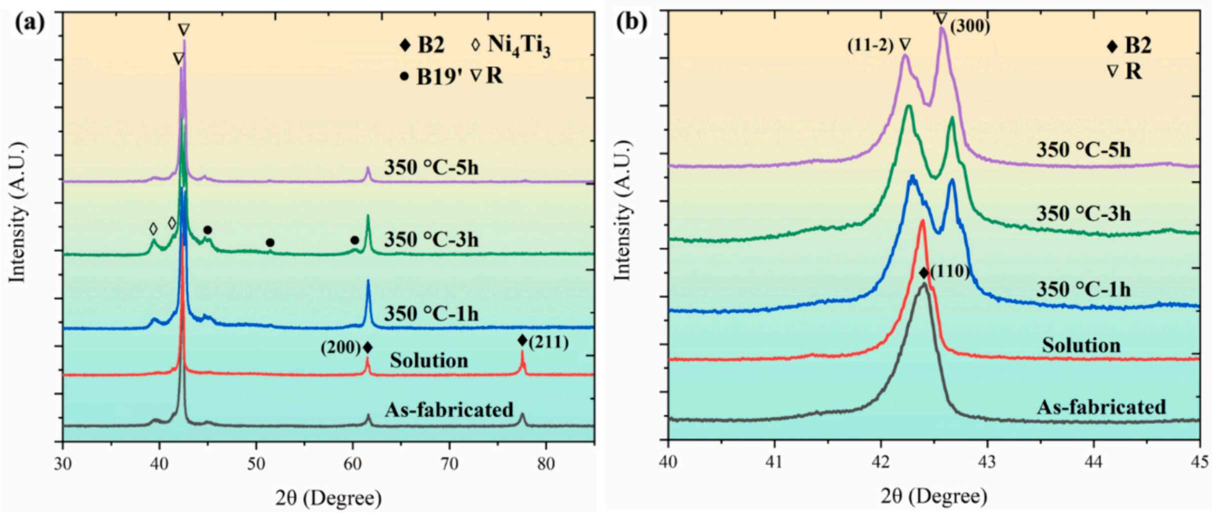

Fig. 2. XRD patterns of the LPBF NiTi in different states.

temperature (A_f) were determined by tangent method [35]. Fig. 3b shows the alteration of M_s, M_f, A_s, and A_f, and Table 1 summaries the TTs of LPBF $Ni_{50.7}Ti_{49.3}$ samples under different states. These TTs decreased after solution treatment significantly. Then, the TTs increased after aging treatment at 350 °C, and with the increase of aging time, the TTs increased gradually. Specifically, TTs decreased by above 30 °C and peaks were sharpened after solution treatment (see the DSC peaks in Fig. 3a). It can be attributed to the elimination of residual thermal stress, formed Ni-rich secondary phase during LPBF process dissolved into matrix, and a more homogeneous and Ni-rich matrix obtained after solution treatment [24,30,37]. As a result, the TTs decreased due to the increase of Ni content in matrix and the peaks became sharper due to the obtained homogenous microstructure and the elimination of residual thermal stress [38].

After aging treatment, the formation of Ni-rich Ni_4Ti_3 precipitate was responsible for the significantly increase of TTs. Specifically, the formation of Ni-rich Ni_4Ti_3 precipitate reduced the Ni content in matrix, thereby increasing the TTs [38,39]. Meanwhile, with the increase of aging time, Ni_4Ti_3 precipitate in the matrix gradually grew and saturated (More details were presented in Fig. 8). Therefore, the increase of TTs was slow, and TTs were close to certain values finally. Besides, a two-step phase transformation behavior can be observed in the LPBF NiTi samples after aging treatment. The aged NiTi samples underwent B19′ → R → B2 during heating, and B2 → B19′ during cooling. It had been demonstrated that the formation of Ni_4Ti_3 precipitate in the matrix of NiTi can promote the occurrence of R phase transformation [40,41]. Thus, the reason behind was supposed to be that Ni_4Ti_3 precipitate acted as a much stronger obstacle to the B2↔B19′ transformation than that to the B2↔R transformation because the former had a much larger transformation strain. Some prior works also manifested that the strain field associated with Ni_4Ti_3 precipitate can promote the occurrence of R phase transformation [4,42]. More details will be shown in Section 3.2.

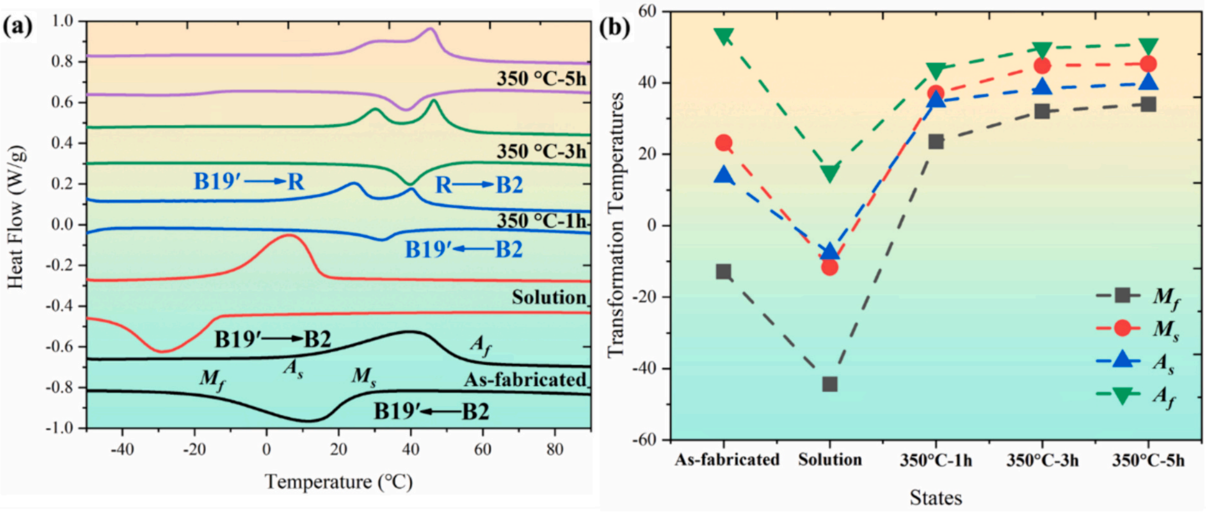

Fig. 3. DSC curves of the LPBF $Ni_{50.7}Ti_{49.3}$ samples in different states.

Table 1
Phase transformation temperatures of LPBF $Ni_{50.7}Ti_{49.3}$ samples under different states.

Sample	Phase Transformation Temperature (°C)					
	M_f	M_s	R_s	R_f	A_s	A_f
As-fabricated	−12.9	23.2	–	–	13.8	53.6
Solution	−44.4	−11.6	–	–	−7.7	15.1
350 °C-1 h	23.5	37.0	15.1	28.6	34.8	43.9
350 °C-3 h	32.0	44.8	20.4	35.3	38.4	49.7
350 °C-5 h	34.0	45.3	24.2	36.7	39.8	50.8

3.2. *Microstructural evolution*

Fig. 4 shows inverse pole figure (IPF) maps and grain diameter distributions obtained by EBSD analysis of the as-fabricated and solution NiTi samples. The average grain size of B2 austenite was 7.6 μm (Fig. 4b) and 25.9 μm (Fig. 4d) for the as-fabricated and solution NiTi samples, respectively. During the aging treatment, the morphology and size of grains in the solution NiTi sample were almost not changed [40,43]. Thus, the IPF maps and grain diameter distributions of aged NiTi samples were not given in this work. Furthermore, the disappearance of partial low angle grain boundaries and substructures during solution treatment made the grain size increased remarkably. Besides, it should be noted that there was no obvious $\langle 100 \rangle_{B2}$ texture in the EBSD analysis, which could technically improve the superelasticity in compression [44].

Fig. 5 exhibits the SEM images of the LPBF $Ni_{50.7}Ti_{49.3}$ samples at different aging treatments. In this work, the aging treatment was designed to introduce different strain fields by tailoring nano-sized Ni_4Ti_3 precipitate in the LPBF NiTi matrix. It is reasonable to deduced that the morphology of grains in all aged NiTi was almost identical with solution treatment NiTi sample. Hence, there was no difference among the overall microstructures in Fig. 5a-c. However, SEM images at high magnifications shows that the content of lath martensite increased with the aging time, as marked by the arrows (Fig. 5d-f). Based on Fig. 5d-f, the image analysis by *ImageJ* software demonstrated that the content of lath martensite were 6.2 %, 7.8 %, and 9.4 % in LPBF NiTi samples aged 1 h, 3 h, and 5 h, respectively. The change of TTs might be a crucial factor for the alteration of lath martensite content [45]. The phase transformation temperatures increased with the increase of the aging time, which made more martensite stable at the room temperature. Thus, more lath martensite formed in LPBF NiTi sample with 5 h aging treatment. More details about microstructure evolution will be characterized by following TEM results.

Fig. 6 exhibits the TEM images of as-fabricated NiTi sample. Distinctly, ultrafine cellular grains (Fig. 6a), dislocations, and Ti_2Ni precipitate (Fig. 6b) were formed in as-fabricated NiTi sample. It is clear that heterogeneous microstructures were observed by TEM results, which was consistent with the IPF map in Fig. 4a. The statistical results show that the size of Ti_2Ni precipitate ranged from 100 nm to 480 nm. The formation of ultrafine cellular grains was attributed to the occurrence of solidification at boundaries of melt pools firstly and high cooling rate. Similar results also had been observed in LPBF and laser-welded NiTi SMAs [34,46]. Meanwhile, the formation of dislocations was related to the occurrence of non-equilibrium rapid solidification and high residual thermal stress in the LPBF process. It is noted that Ti_2Ni precipitate was generated in the B2 matrix (Fig. 6b), similar to that in LPBF $Ni_{50.66}Ti_{49.34}$ SMA [47].

Fig. 7 shows TEM images of aged NiTi samples. It is found that nano-sized Ni_4Ti_3 precipitate was formed in the matrix of all aged NiTi samples (Fig. 7a-c). Further high-resolution TEM images in Fig. 7d-f show that the size of the Ni_4Ti_3 precipitate increased with the aging time. In a comparative analysis of the nano-sized Ni_4Ti_3 precipitate in the three aged NiTi samples, it is interesting to find that they had different morphologies and sizes. The nano-sized Ni_4Ti_3 precipitate exhibited spherical (Fig. 7d), ellipsoidal (Fig. 7e), and lenticular (Fig. 7f) morphologies in aged NiTi samples. Meanwhile, the size of Ti_2Ni precipitate in aged NiTi samples ranged from 200 nm to 800 nm. It is found that the size of Ti_2Ni precipitate was bigger after solution and aging treatment. According to Ni—Ti binary phase diagram, the Ti_2Ni precipitate dissolves into the matrix when the temperature exceeds 984 °C. In this work, the temperature of solution treatment is 950 °C. The Ti_2Ni precipitate at as-fabricated NiTi sample cannot dissolve into the matrix, and the diffusion of supersaturated Ti atoms in the matrix promoted the growth of Ti_2Ni precipitate during solution and subsequent aging treatment. Thus, the size of Ti_2Ni precipitate increased after solution and aging treatment [28]. Furthermore, the strain fields from different morphologies and sizes of Ni_4Ti_3 nanoprecipitate might be associated with different superelasticity of the three aged NiTi samples, as explained in Section 4.2.

3.3. *Superelasticity*

Fig. 8 shows the superelasticity of LPBF NiTi samples at different states. In the experiment of as-fabricated NiTi sample, the loading stress was 800 MPa, and the applied stress was 600 MPa in other samples. There were significant differences in superelasticity of the NiTi samples

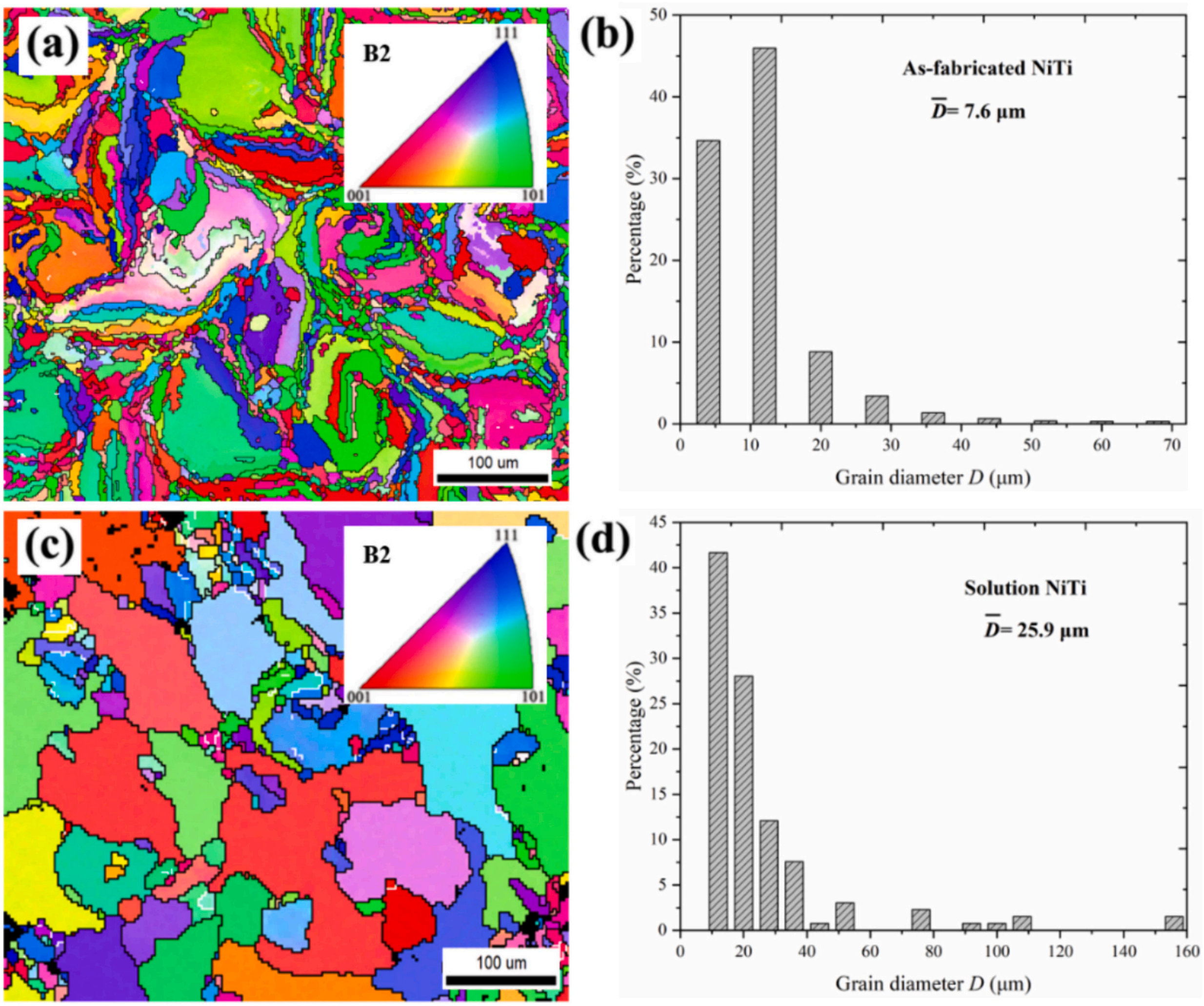

Fig. 4. IPF maps and grain diameter distribution of XY plane for the LPBF $Ni_{50.7}Ti_{49.3}$ SMA samples at different states: (a, b) As-fabricated, (c, d) Solution.

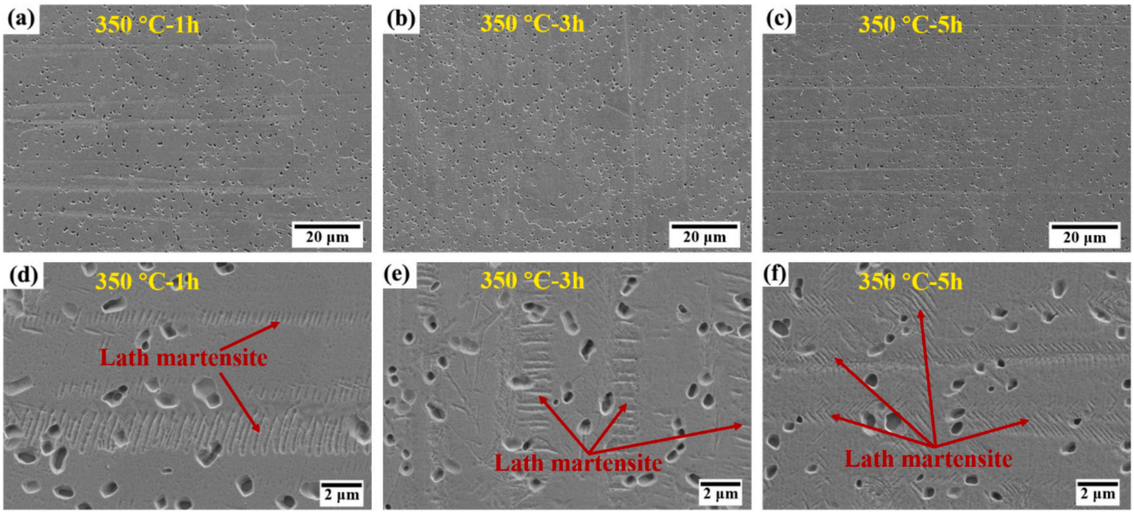

Fig. 5. SEM images of XY planes for LPBF $Ni_{50.7}Ti_{49.3}$ samples at different aging treatments: (a, d) 350 °C-1 h, (b, e) 350 °C-3 h, (c, f) 350 °C-5 h.

based on Fig. 8. Fig. 9a shows the schematic diagram of obtaining total strain (ε_{tot}), recovery strain (ε_{rec}), residual strain (ε_{res}), and recovery tare ($\eta = \varepsilon_{rec}/\varepsilon_{max} \times 100$ %) at the 1st and 10th cycles. Fig. 9a also shows the method to obtain the critical stress of stress-induced martensite transformation (σ_{SIM}). To intuitively observe the changes in recovery strain and recovery ratio as functions of the cycle number N, the related quantities associated with the superelasticity are presented in Fig. 9b and c. Fig. 9d shows the recovery strain-recovery rate results of

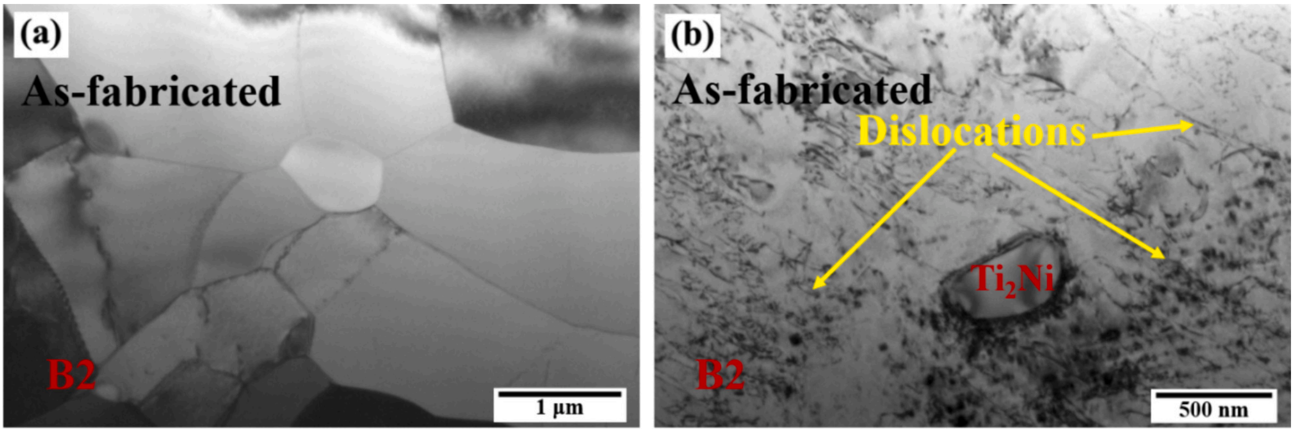

Fig. 6. TEM images of as-fabricated NiTi sample: (a) ultrafine cellular grains and (b) dislocations and Ti_2Ni precipitate.

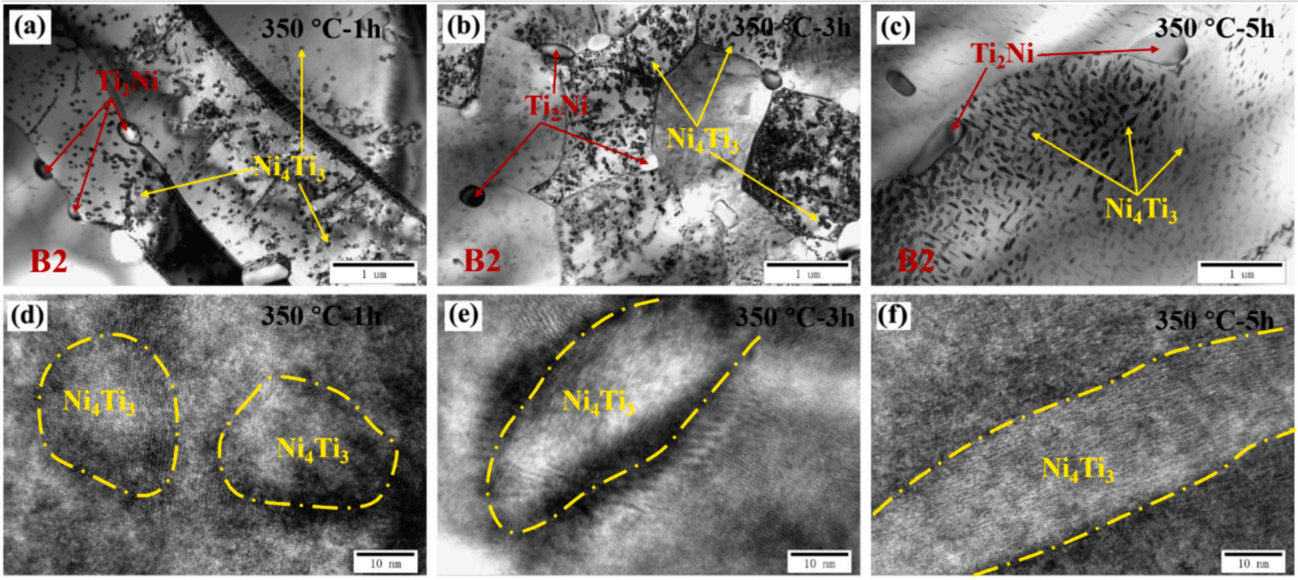

Fig. 7. TEM and HRTEM images of the LPBF $Ni_{50.7}Ti_{49.3}$ samples at different aging treatments: (a, d) 350 °C-1 h, (b, e) 350 °C-3 h, (c, f) 350 °C-5 h.

representative NiTi SMAs obtained by LPBF. The ε_{tot}, ε_{rec}, and η for LPBF NiTi samples were summarized in Table 2.

The as-fabricated NiTi sample showed recovery strain of 5.03 % in 1st cycle and recovery strain of 3.81 % in 10th cycle (Table 2). It is clear that the as-fabricated NiTi sample showed worst superelasticity stability. Specifically, the recovery rate decreased from 76.0 % to 52.3 % during cycle compressive test (Table 2). The remarkable degeneration of recovery strain was attributed to the occurrence of dislocation motion and formation of retained stabilized martensite plates in the matrix [45]. After solution and aging treatment, the recovery strains and recovery rates were higher than that of the as-fabricated NiTi sample. Specifically, for the 350 °C-1 h NiTi sample, the recovery strain decreased slowly with the increase of cycle number N, the recovery strains were 6.39 % and 6.07 % in 1st and 10th cycle, respectively, which showed 0.32 % degeneration of recovery strain during compressive test. Besides, based on Table 2, 350 °C-3 h and 350 °C-5 h NiTi samples obtained more stable recovery strains than that of 350 °C-1 h NiTi sample. Almost no change in the recovery strains was observed in these two aged NiTi samples. At 10th cycle, all aged NiTi samples obtained recovery rates above 99 %, which were much better than that of the as-fabricated NiTi sample in this work and prior works [11,29,30,34,44,47–53] (Fig. 9d), including LPBF $Ni_{50.8}Ti_{49.2}$ SMAs containing single B2 austenite or exhibiting a strong $<100>_{B2}$ texture [44,49]. Interestingly, the ε_{rec} and η of aged NiTi samples was always far higher than that of as-fabricated NiTi sample, regardless of N (Fig. 9b and c), and the maximum ε_{rec} obtained in aged NiTi samples was 6.39 %. Therefore, the ultrahigh ε_{rec} reported in this work suggested that the tailoring strain field by Ni_4Ti_3 precipitate in LPBF NiTi SMAs made it available for excellent superelasticity. Furthermore, the underlying mechanism for the alteration of superelasticity obtained among LPBF NiTi samples will be discussed in Section 4.2.

4. Discussion

4.1. Effect of post heat treatments on microstructure evolution

Fig. 10 shows the alteration of σ_{SIM}. It is clear that the as-fabricated NiTi sample exhibited highest σ_{SIM} (562 MPa). This was also the reason for its higher loading stress at cycle compressive test in Fig. 8. The residual thermal stress produced during LPBF process might the reason for highest σ_{SIM} in as-fabricated NiTi sample. After solution and aging treatment, the σ_{SIM} of 350 °C-1 h, 350 °C-3 h, and 350 °C-5 h NiTi samples were 295 MPa, 306 MPa, and 309 MPa, respectively, which was much smaller than that of as-fabricated NiTi sample. This result indicated that the heat treatment was effective to weaken or eliminate the residual thermal stress. Besides, in this work, the rate of Ni and Ti is

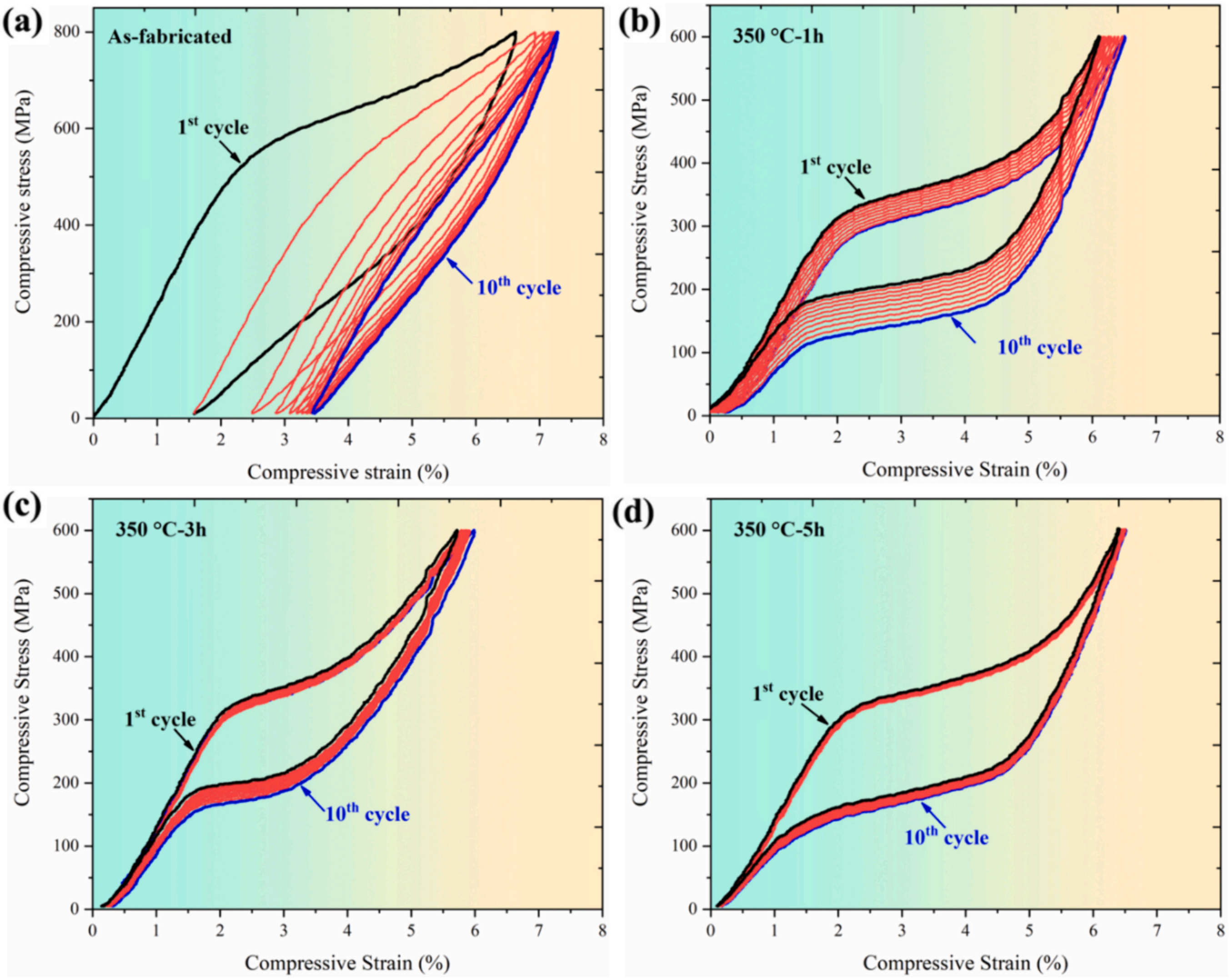

Fig. 8. The superelasticity of LPBF $Ni_{50.7}Ti_{49.3}$ under different states at $A_f + 10$ °C: (a) As-fabricated, (b) 350 °C-1 h, (c) 350 °C-3 h, (d) 350 °C-5 h.

50.7: 49.3. For the as-fabricated NiTi sample, the cooling rate of melt pools might be 10^4–10^6 °C/s, this high cooling rate and short cooling time might make the matrix would form a Ni atom supersaturated solid solution during LPBF process. Thus, the supersaturated Ni atoms would result in Ni doping in the B2 austenite matrix for the as-fabricated NiTi sample. The strain field produced by Ni doping in the matrix can significantly inhibit martensite transformation and increase martensite transformation resistance [54,55], which might be the reason for the high σ_{SIM} of as-fabricated $Ni_{50.7}Ti_{49.3}$ sample in this study.

Figs. 4–7 show the microstructure of LPBF NiTi samples under different states. The microstructure evolution was obvious after solution and aging treatment. After aging treatment, the characteristics of Ni_4Ti_3 precipitate were summarized in Table 3. The Ni_4Ti_3 precipitate changed from spherical shape to ellipsoidal shape and lenticular shape with the increase of aging time (Fig. 7). Meanwhile, the size of Ni_4Ti_3 precipitate increased with the increase of aging time. Besides, the interval of interparticle spacing in NiTi sample under 350 °C -1 h aging treatment showed the maximum value (Table 3). It meant that the precipitation of Ni_4Ti_3 exhibited uneven distribution compared with other two aged NiTi samples. The relatively low aging temperature and short aging time might be the reason for the occurrence of this result, which could lead the incomplete precipitation of Ni_4Ti_3 and relatively low-density of Ni_4Ti_3 (~608 μm^{-2}) in 350 °C -1 h aged NiTi sample. As the aging time increased to 3 h, the density of Ni_4Ti_3 became ~880 μm^{-2}, and the interval of interparticle spacing decreased (Table 3). This indicated that the distribution of Ni_4Ti_3 was more uniform. When the aging time increased to 5 h, it is found that the width of Ni_4Ti_3 precipitate hardly changed, and the length increased remarkably. The lenticular Ni_4Ti_3 formed in the NiTi matrix, similar results also observed in other NiTi SMAs [40,56,57]. As the size of Ni_4Ti_3 increased, the density of Ni_4Ti_3 changed from ~880 μm^{-2} (350 °C-3 h) to ~790 μm^{-2} (350 °C-5 h).

4.2. The mechanism of enhanced superelasticity

Figs. 8 and 9 show the alteration of superelasticity for LPBF NiTi samples. After solution and aging treatment, the superelasticity were improved significantly compared with that of as-fabricated NiTi sample. Although the recovery rate increased with the increase of cycle number during compressive test, the recovery strain of 350 °C-1 h NiTi sample showed 0.32 % degeneration during compressive test. The characteristics of strain field from Ni_4Ti_3 precipitate were the crucial factor for this degeneration. Prior simulation results proved that the strain field in the vicinity of the precipitate-matrix interface could reach up to maximized value when the nano-sized Ni_4Ti_3 precipitate was spherical [58]. Fig. 11 shows HRTEM images, fast Fourier transform, and strain tensor components of 350 °C-1 h, 350 °C-3 h, 350 °C-5 h NiTi samples, and Table 4 summaries the average lattice strain components determined from the yellow solid line square areas (5 nm × 5 nm) indicated in Fig. 11a, d, and

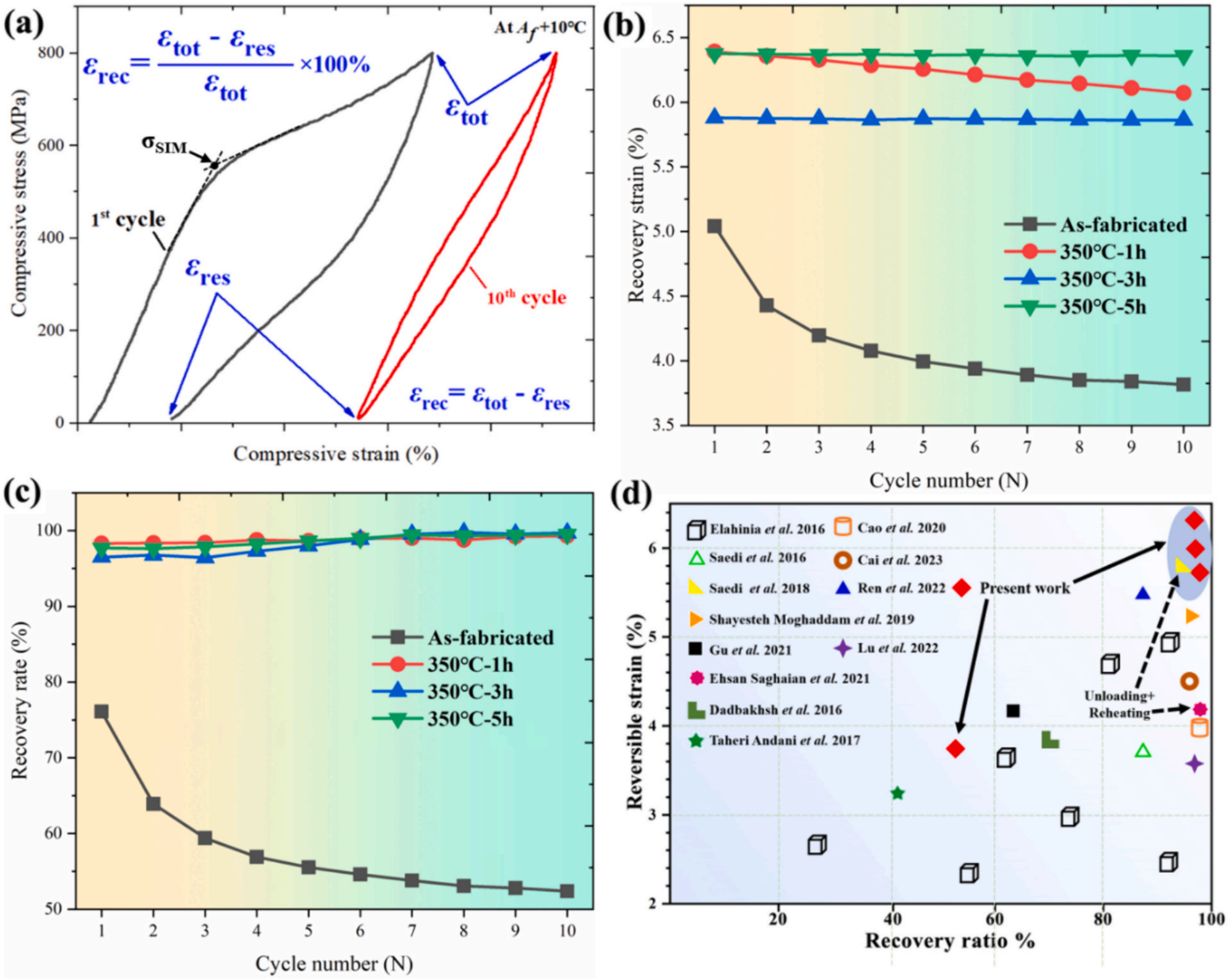

Fig. 9. (a) The schematic diagram to analyze superelasticity, the alteration of recovery strain (b) and recovery rate (c) with cycle number during compressive test of LPBF $Ni_{50.7}Ti_{49.3}$ samples at different states, (d) Recovery strain-recovery rate results of representative NiTi SMAs obtained by LPBF [11,29,30,34,44,47–53].

Table 2
Summary of cycle superelasticity of LPBF NiTi samples.

Samples	1st cycle			10th cycle		
	ε_{tot} (%)	ε_{rec} (%)	η (%)	ε_{tot} (%)	ε_{rec} (%)	η (%)
As-fabricated	6.62	5.03	76.0 %	7.28	3.81	52.3
350 °C-1 h	6.50	6.39	98.3	6.11	6.07	99.3
350 °C -3 h	6.07	5.88	96.5	5.90	5.86	99.7
350 °C -5 h	6.51	6.38	97.7	6.41	6.36	99.5

g. In this work, it is reasonable to deduce that the lattice strain components were consistent with the strain fields.

As shown in Fig. 11c, f, and i, ε_{xx} in the B2 phase were larger than those in the Ni_4Ti_3 precipitate. Specifically, a quantitative analysis revealed that the average ε_{xx} in the B2 phase were 0.15 %, 0.13 % and 0.10 % for the 350 °C-1 h, 350 °C-3 h, 350 °C-5 h NiTi samples, respectively. On the other hand, the average ε_{xx} in the Ni_4Ti_3 precipitate were − 0.12 %, −0.24 % and − 0.28 % for the 350 °C-1 h, 350 °C-3 h, 350 °C-5 h NiTi samples, respectively. These values were indicative of a tensile strain state in the B2 matrix and a compressive strain state in the Ni_4Ti_3 precipitate, which was consistent with the prior experimental and simulation results [4,58,59]. Based on Table 4, it can be found that the ε_{xx} in B2 phase decreased when the morphology of Ni_4Ti_3 changed from spherical shape to ellipsoidal, and lenticular shape. However, the absolute value of the ε_{xx} in Ni_4Ti_3 precipitate showed an opposite change rule. In this work, the loading stress was 600 MPa for aged NiTi samples.

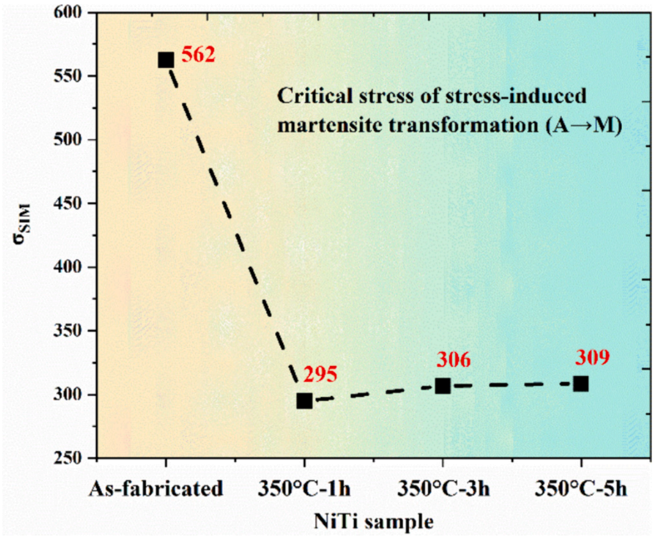

Fig. 10. The alteration of critical stress of stress-induced martensite transformation (σ_{SIM}) for LPBF $Ni_{50.7}Ti_{49.3}$ samples at different states.

For 350 °C-1 h aged NiTi sample, although the strain field in B2 matrix introduced by Ni_4Ti_3 precipitate was maximum (0.15 %), it can be deduced that the loading stress of 600 MPa was larger than the strength

Table 3

Characteristics of Ni_4Ti_3 precipitate formed in aged NiTi samples. *L*: length; *W*: width; *D*: interparticle spacing; *ρ*: density.

Samples	*L* (nm)	*W* (nm)	*D* (nm)	*ρ* (μm^{-2})
350 °C-1 h	20–35	18–34	8–400	608
350 °C-3 h	55–160	28–40	30–100	880
350 °C-5 h	70–200	25–55	35–80	790

of this strain field [36]. The formed dislocations would break through the obstruction of strain field and cut-through coherent spherical Ni_4Ti_3 precipitate gradually instead of impede by this strain field in prior work [36]. Thus, the spherical Ni_4Ti_3 precipitate showed a relatively low obstruction for dislocation motion during cycle compressive loading at 600 MPa. Besides, short aging time resulted in the formation of non-uniformly distributed Ni_4Ti_3 precipitate in matrix (Fig. 7 and Table 4), which caused the differences in the strength of matrix, and the relatively easy occurrence of dislocation formation and motion. Thus, a gradually decreasing recovery strain and 0.32 % degeneration of recovery strain obtained in 350 °C-1 h aged NiTi sample.

When the aging time increased to 3 h and 5 h, the Ni_4Ti_3 precipitate became ellipsoidal and lenticular shape, and the density reached 880 μm^{-2} and 790 μm^{-2}, respectively. Meanwhile, with the increase of aging time, the size of Ni_4Ti_3 increased dramatically. It had been confirmed that the interface between the B2 matrix and Ni_4Ti_3 precipitate changed from coherent to semi-coherent, and non-coherent relationship with the increasing size of Ni_4Ti_3 precipitate [60]. With the increase of aging

Table 4

Average lattice strain components determined from the yellow solid line square areas (5 nm × 5 nm) indicated in Fig. 11.

Sample	B2 (ε_{xx})	Ni_4Ti_3 (ε_{xx})	Interface zone (ε_{xx})
350 °C-1 h	0.15 %	−0.12 %	0.03 %
350 °C-3 h	0.13 %	−0.24 %	−0.08 %
350 °C-5 h	0.10 %	−0.28 %	−0.09 %

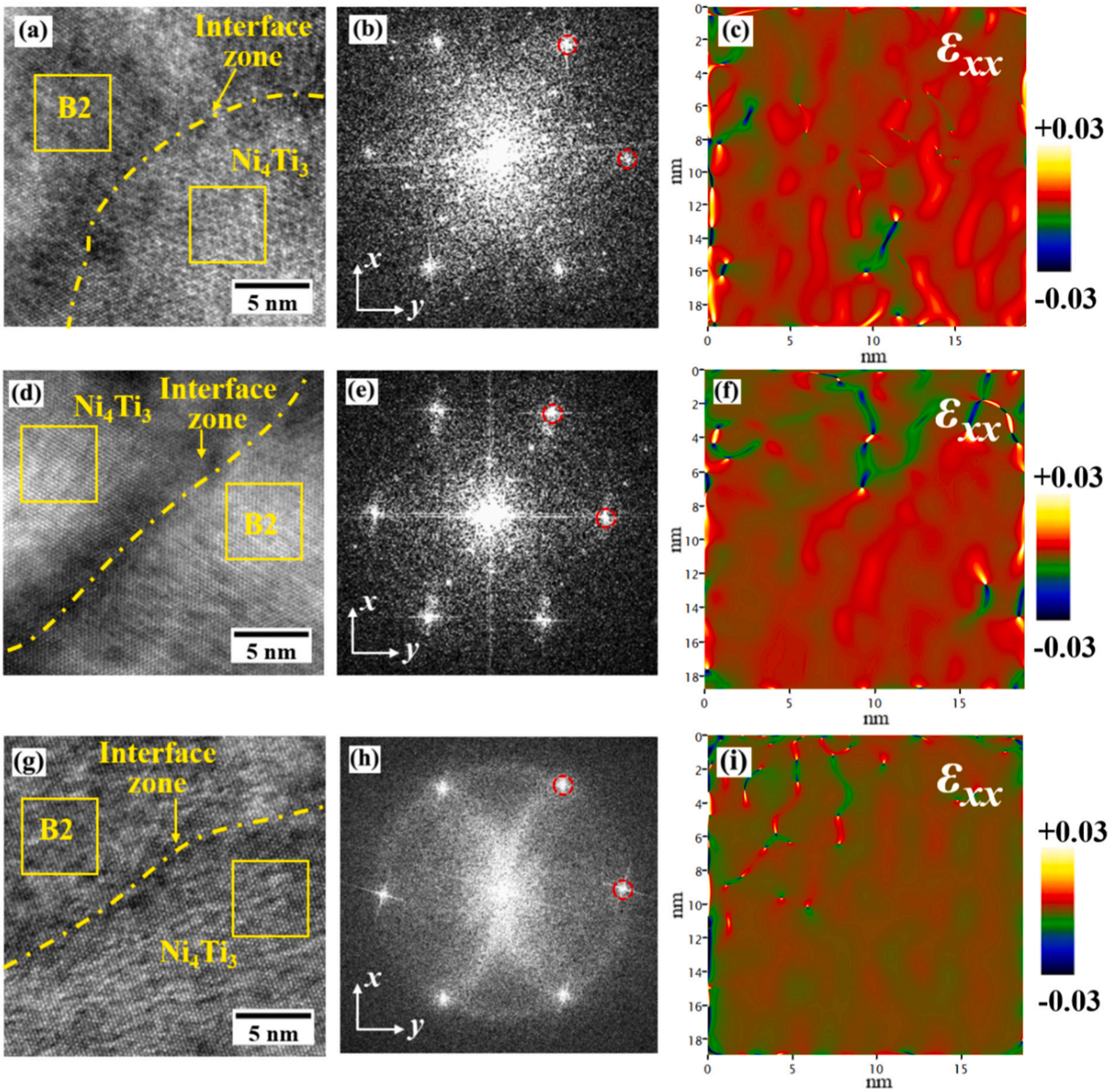

Fig. 11. HRTEM images, fast Fourier transform, and strain tensor components of 350 °C-1 h (a-c), 350 °C-3 h (d-f), 350 °C-5 h (g-i) $Ni_{50.7}Ti_{49.3}$ samples. The strain tensor components ε_{xx} obtained using GPA: x // $[1\bar{1}0]_{B2}$, y // $[10\bar{1}]_{B2}$. The g-vectors marked by the red circles in (b), (e), and (h) were used for calculating the strain tensor components. (For interpretation of the references to colour in this figure legend, the reader is referred to the web version of this article.)

times were 3 h and 5 h, the length of Ni_4Ti_3 could reach about 200 nm (Fig. 7 and Table 4), the strain field in B2 phase around the precipitate-matrix interface decreased in these two NiTi samples (Fig. 11). However, because the precipitation behavior of Ni_4Ti_3 reached an equilibrium and uniformly distributed state approximately, there was relatively uniform strain field in 350 °C-3 h and 350 °C-5 h NiTi samples. This might result in the formation of dislocations more difficult in above two NiTi samples than that in 350 °C-1 h NiTi sample during loading. The large, uniformly distributed, and high-density Ni_4Ti_3 precipitate in these two NiTi samples enhanced the matrix by precipitation hardening remarkably, which improved the strength of the matrix significantly [61–64]. Furthermore, a large number of semi-coherent and non-coherent interfaces hindered the generated dislocation motion effectively during loading test. Hence, the plastic deformation generated during cyclic compression was impeded, and resulting in the occurrence of stable stress-induced martensite transformation in these two aged NiTi sample, and obtaining excellent recovery strain and recovery rate. In addition, previous studies had also demonstrated that the volume fraction and size of formed nano-precipitate can significantly improve the recovery strain of NiTi samples [65,66]. Thus, a recovery strain >6 % was obtained during 10th cycle of compression. Besides, compared with prior works [36], the aged NiTi samples seemed to show asymmetrical superelasticity under tensile and compressive states of deformation, the altered various number of twinning modes, martensite slip and hardening effects might be responsible for the tension-compression asymmetry, which needed to be studied in LPBF NiTi SMAs systematically in future works.

5. Conclusions

In this work, a $Ni_{50.7}Ti_{49.3}$ shape memory alloy was fabricated by LPBF, and excellent superelasticity was obtained by tailoring strain field from Ni_4Ti_3 precipitate in LPBF $Ni_{50.7}Ti_{49.3}$. The underlying mechanisms for the altered superelasticity of LPBF $Ni_{50.7}Ti_{49.3}$ samples was studied systematically. The conclusions were as followings:

1. The Ni_4Ti_3 nano-precipitates with different spherical, ellipsoidal, and lenticular morphologies in the LPBF and heat-treated NiTi samples show 0.15 %, 0.13 %, and 0.10 % strain field around Ni_4Ti_3 nano-precipitates in B2 matrix, respectively.
2. The NiTi sample with spherical Ni_4Ti_3 nano-precipitate and highest strain field displays the worst superelasticity stability, which was originated from its spherical Ni_4Ti_3 nano-precipitate cut through by dislocations due to coherent interface between the spherical nano-precipitate and B2 matrix.
3. The NiTi sample with lenticular Ni_4Ti_3 nano-precipitate and smallest strain field exhibits the biggest superelasticity of 6.36 %, which was attributed to effectively impediment of simi-coherent or non-coherent interface between the lenticular Ni_4Ti_3 nano-precipitate and B2 matrix for dislocations motion.
4. The LPBF NiTi samples with proper heat treatment could present >6 % recovery strain together with >99 % recovery rate during 10-times cyclic compression loading, although different mechanisms between the Ni_4Ti_3 nano-precipitates and generated dislocations during cyclic loading and different interfaces between the Ni_4Ti_3 nano-precipitates and B2 matrix in the NiTi samples.

CRediT authorship contribution statement

H.Z. Lu: Writing – review & editing, Funding acquisition, Formal analysis. **Y. Luo:** Methodology, Data curation. **T.H. Long:** Validation. **W.T. Tong:** Supervision. **Y. Zhang:** Visualization. **X. Yu:** Project administration, Data curation. **C. Yang:** Writing – review & editing, Resources, Funding acquisition.

Declaration of competing interest

The authors declare that they have no known competing financial interests or personal relationships that could have appeared to influence the work reported in this paper.

Acknowledgments

This work was supported by the National Natural Science Foundation of China (No. 52371027), the Key-Area Research and Development Program of Guangdong Province (Nos. 2020B090923001 and 2022B1515120082), Guangdong Science and Technology Innovation Project (No. 2021TX06C111), Guangdong Basic and Applied Basic Research Foundation (No. 2023A1515111113), Guangzhou Science and Technology Planning Project (No. 2024A04J4754), and the Opening Foundation of State Key Laboratory of Metastable Materials Science and Technology, Yanshan University (No. 202302).

References

[1] Ke W, Yan W, Oliveira JP, Pang B, Chen L, Wu Y, et al. Thermal-fluid behavior, microstructure and mechanical properties in liquid bridge transfer mode during directed energy deposition-arc additive manufacturing – insights using NiTi as a model alloy. Addit Manuf 2023;77:103807.
[2] Teshome FB, Peng B, Oliveira JP, Shen J, Ao S, Li H, et al. Role of Pd interlayer on NiTi to Ti6Al4V laser welded joints: microstructural evolution and strengthening mechanisms. Mater Des 2023;228:111845.
[3] Hussain S, Alagha AN, Haidemenopoulos GN, Zaki W. Microstructural and surface analysis of NiTi TPMS lattice sections fabricated by laser powder bed fusion. J Manuf Process 2023;102:375–86.
[4] Tirry W, Schryvers D. Linking a completely three-dimensional nanostrain to a structural transformation eigenstrain. Nat Mater 2009;8(9):752–7.
[5] Wang X, Pu Z, Yang Q, Huang S, Wang Z, Kustov S, et al. Improved functional stability of a coarse-grained Ti-50.8 at.% Ni shape memory alloy achieved by precipitation on dislocation networks. Scr Mater 2019;163:57–61.
[6] Yamamoto T, Kato H, Murakami Y, Kimura H, Inoue A. Martensitic transformation and microstructure of Ti-rich Ti-Ni as-atomized powders. Acta Mater 2008;56(20):5927–37.
[7] Tomozawa M, Kim HY, Miyazaki S. Shape memory behavior and internal structure of Ti-Ni-cu shape memory alloy thin films and their application for microactuators. Acta Mater 2009;57(2):441–52.
[8] Chang SH, Wu SK, Wu LM. Shape memory characteristics of as-spun and annealed $Ti_{51}Ni_{49}$ crystalline ribbons. Intermetallics 2010;18(5):965–71.
[9] A. Ishida, M. Sato, S. Miyazaki, Mechanical properties of Ti-Ni shape memory thin films formed by sputtering, Mater Sci Eng A 273–275 (1999) 754–757.
[10] Tadayyon G, Mazinani M, Guo Y, Zebarjad SM, Tofail SAM, Biggs MJ. The effect of annealing on the mechanical properties and microstructural evolution of Ti-rich NiTi shape memory alloy. Mater Sci Eng A 2016;662:564–77.
[11] Elahinia M, Shayesteh Moghaddam N, Taheri Andani M, Amerinatanzi A, Bimber BA, Hamilton RF. Fabrication of NiTi through additive manufacturing: a review. Prog Mater Sci 2016;83:630–63.
[12] Yu Z, Xu Z, Guo Y, Sha P, Liu R, Xin R, et al. Analysis of microstructure, mechanical properties, wear characteristics and corrosion behavior of SLM-NiTi under different process parameters. J Manuf Process 2022;75:637–50.
[13] Shi G, Li L, Yu Z, Liu R, Sha P, Xu Z, et al. The interaction effect of process parameters on the phase transformation behavior and tensile properties in additive manufacturing of Ni-rich NiTi alloy. J Manuf Process 2022;77:539–50.
[14] Elahinia MH, Hashemi M, Tabesh M, Bhaduri SB. Manufacturing and processing of NiTi implants: a review. Prog Mater Sci 2012;57(5):911–46.
[15] Lu HZ, Ma HW, Luo X, Wang Y, Wang J, Lupoi R, et al. Microstructure, shape memory properties, and in vitro biocompatibility of porous NiTi scaffolds fabricated via selective laser melting. J Mater Res Technol 2021;15:6797–812.
[16] Tan C, Li S, Essa K, Jamshidi P, Zhou K, Ma W, et al. Laser powder bed fusion of Ti-rich TiNi lattice structures: process optimisation, geometrical integrity, and phase transformations. Int J Mach Tool Manuf 2019;141:19–29.
[17] Sun L, Chen K, Geng P, Zhou Y, Wen S, Shi Y. Mechanical and shape memory properties of NiTi triply periodic minimal surface structures fabricated by laser powder bed fusion. J Manuf Process 2023;101:1091–100.
[18] Das M, Balla VK, Basu D, Bose S, Bandyopadhyay A. Laser processing of SiC-particle-reinforced coating on titanium. Scr Mater 2010;63(4):438–41.
[19] Luo X, Song T, Gebert A, Neufeld K, Kaban I, Ma H, et al. Programming crystallographic orientation in additive-manufactured beta-type titanium alloy. Adv Sci 2023;10:2302884.
[20] Parry L, Ashcroft IA, Wildman RD. Understanding the effect of laser scan strategy on residual stress in selective laser melting through thermo-mechanical simulation. Addit Manuf 2016;12:1–15.
[21] Cheng B, Shrestha S, Chou K. Stress and deformation evaluations of scanning strategy effect in selective laser melting. Addit Manuf 2016;12:240–51.

[22] Gu D, Ma C. In-situ formation of Ni_4Ti_3 precipitate and its effect on pseudoelasticity in selective laser melting additive manufactured NiTi-based composites. Appl Surf Sci 2018;441:862–70.

[23] Xue L, Atli KC, Zhang C, Hite N, Srivastava A, Leff A, et al. Laser powder bed fusion of defect-free NiTi shape memory alloy parts with superior tensile Superelasticity. Acta Mater 2022;229:117781.

[24] Franco BE, Ma J, Loveall B, Tapia GA, Karayagiz K, Liu J, et al. A sensory material approach for reducing variability in additively manufactured metal parts. Sci Rep 2017;7(1):3604.

[25] Sam J, Franco B, Ma J, Karaman I, Elwany A, Mabe JH. Tensile actuation response of additively manufactured nickel-titanium shape memory alloys. Scr Mater 2018;146:164–8.

[26] Li S, Hassanin H, Attallah MM, Adkins NJE, Essa K. The development of TiNi-based negative Poisson's ratio structure using selective laser melting. Acta Mater 2016;105:75–83.

[27] Tan C, Zou J, Li S, Jamshidi P, Abena A, Forsey A, et al. Additive manufacturing of bio-inspired multi-scale hierarchically strengthened lattice structures. Int J Mach Tool Manuf 2021;167:103764.

[28] Lu HZ, Liu LH, Yang C, Luo X, Song CH, Wang Z, et al. Simultaneous enhancement of mechanical and shape memory properties by heat-treatment homogenization of Ti_2Ni precipitates in TiNi shape memory alloy fabricated by selective laser melting. J Mater Sci Technol 2022;101:205–16.

[29] Cao Y, Zhou X, Cong D, Zheng H, Cao Y, Nie Z, et al. Large tunable elastocaloric effect in additively manufactured Ni-Ti shape memory alloys. Acta Mater 2020;194:178–89.

[30] Saedi S, Turabi AS, Taheri Andani M, Haberland C, Karaca H, Elahinia M. The influence of heat treatment on the thermomechanical response of Ni-rich NiTi alloys manufactured by selective laser melting. J Alloys Compd 2016;677:204–10.

[31] Saedi S, Turabi AS, Andani MT, Moghaddam NS, Elahinia M, Karaca HE. Texture, aging, and superelasticity of selective laser melting fabricated Ni-rich NiTi alloys. Mater Sci Eng A 2017;686:1–10.

[32] Yang C, Lu HZ, Ma HW, Cai WS. Research and Development in NiTi shape memory alloys fabricated by selective laser melting. Acta Metall Sin 2023;59(1):55–74.

[33] Gu D, Hagedorn Y-C, Meiners W, Meng G, Batista RJS, Wissenbach K, et al. Densification behavior, microstructure evolution, and wear performance of selective laser melting processed commercially pure titanium. Acta Mater 2012;60(9):3849–60.

[34] Cai WS, Luo Y, Yan A, Kang LM, Zhang LC, Suryanarayana C, et al. Balanced strength-ductility combination and good recoverable strain of $Ni_{50.7}Ti_{49.3}$ alloy fabricated by high scanning velocity in selective laser melting. Mater Charact 2023;195:112490.

[35] Otsuka K, Ren X. Physical metallurgy of Ti-Ni-based shape memory alloys. Prog Mater Sci 2005;50(5):511–678.

[36] Lu HZ, Ma HW, Cai WS, Luo X, Wang Z, Song CH, et al. Stable tensile recovery strain induced by a Ni_4Ti_3 nanoprecipitate in a $Ni_{50.4}Ti_{49.6}$ shape memory alloy fabricated via selective laser melting. Acta Mater 2021;219:117261.

[37] Zhang Q, Hao S, Liu Y, Xiong Z, Guo W, Yang Y, et al. The microstructure of a selective laser melting (SLM)-fabricated NiTi shape memory alloy with superior tensile property and shape memory recoverability. Appl Mater Today 2020;19:100547.

[38] Frenzel J, George EP, Dlouhy A, Somsen C, Wagner MFX, Eggeler G. Influence of Ni on martensitic phase transformations in NiTi shape memory alloys. Acta Mater 2010;58(9):3444–58.

[39] Frenzel J, Wieczorek A, Opahle I, Maaß B, Drautz R, Eggeler G. On the effect of alloy composition on martensite start temperatures and latent heats in Ni-Ti-based shape memory alloys. Acta Mater 2015;90:213–31.

[40] Liu S, Lin Y, Wang G, Wang X. Effect of varisized Ni_4Ti_3 precipitate on the phase transformation behavior and functional stability of Ti-50.8 at.% Ni alloys. Mater Charact 2021;172:110832.

[41] Zhu J, Wu H-H, Wu Y, Wang H, Zhang T, Xiao H, et al. Influence of Ni_4Ti_3 precipitation on martensitic transformations in NiTi shape memory alloy: R phase transformation. Acta Mater 2021;207:116665.

[42] Tirry W, Schryvers D. Quantitative determination of strain fields around Ni_4Ti_3 precipitates in NiTi. Acta Mater 2005;53(4):1041–9.

[43] Radi A, Khalil-Allafi J, Etminanfar MR, Pourbabak S, Schryvers D, Amin-Ahmadi B. Influence of stress aging process on variants of nano-Ni_4Ti_3 precipitates and martensitic transformation temperatures in NiTi shape memory alloy. Mater Des 2018;142:93–100.

[44] Shayesteh Moghaddam N, Saedi S, Amerinatanzi A, Hinojos A, Ramazani A, Kundin J, et al. Achieving superelasticity in additively manufactured NiTi in compression without post-process heat treatment. Sci Rep 2019;9(1):41.

[45] Lu HZ, Ma HW, Yang Y, Cai WS, Luo X, Yan A, et al. Tailoring phase transformation behavior, microstructure, and superelasticity of NiTi shape memory alloys by specific change of laser power in selective laser melting. Mater Sci Eng A 2023;864:144576.

[46] Oliveira JP, Miranda RM, Braz Fernandes FM. Welding and joining of NiTi shape memory alloys: a review. Prog Mater Sci 2017;88:412–66.

[47] Gu D, Ma C, Dai D, Yang J, Lin K, Zhang H, et al. Additively manufacturing-enabled hierarchical NiTi-based shape memory alloys with high strength and toughness. Virtual Phys Prototyp 2021;16(sup1):S19–38.

[48] Lu HZ, Chen T, Liu LH, Wang H, Luo X, Song CH, et al. Constructing function domains in NiTi shape memory alloys by additive manufacturing. Virtual Phys Prototyp 2022;17(3):563–81.

[49] Ehsan Saghaian S, Nematollahi M, Toker G, Hinojos A, Shayesteh Moghaddam N, Saedi S, et al. Effect of hatch spacing and laser power on microstructure, texture, and thermomechanical properties of laser powder bed fusion (L-PBF) additively manufactured NiTi. Opt Laser Technol 2021;149:107680.

[50] Ren Q, Chen C, Lu Z, Wang X, Lu H, Yin S, et al. Effect of a constant laser energy density on the evolution of microstructure and mechanical properties of NiTi shape memory alloy fabricated by laser powder bed fusion. Opt Laser Technol 2022;152:108182.

[51] Dadbakhsh S, Vrancken B, Kruth JP, Luyten J, Van Humbeeck J. Texture and anisotropy in selective laser melting of NiTi alloy. Mater Sci Eng A 2016;650:225–32.

[52] Taheri Andani M, Saedi S, Turabi AS, Karamooz MR, Haberland C, Karaca HE, et al. Mechanical and shape memory properties of porous $Ni_{50.1}Ti_{49.9}$ alloys manufactured by selective laser melting. J Mech Behav Biomed Mater 2017;68:224–31.

[53] Saedi S, Shayesteh Moghaddam N, Amerinatanzi A, Elahinia M, Karaca HE. On the effects of selective laser melting process parameters on microstructure and thermomechanical response of Ni-rich NiTi. Acta Mater 2018;144:552–60.

[54] Qin S-J, Shang J-X, Wang F-H, Chen Y. The role of strain glass state in the shape memory alloy Ni50+Ti50−: insight from an atomistic study. Mater Des 2017;120:238–54.

[55] Yang Y, Xue D, Yuan R, Zhou Y, Sun J. Doping effects of point defects in shape memory alloys. Acta Mater 2019;176:177–88.

[56] Li X, Chen H, Guo W, Guan Y, Wang Z, Zeng Q, et al. Improved superelastic stability of NiTi shape memory alloys through surface nano-crystallization followed by low temperature aging treatment. Intermetallics 2021;131:107114.

[57] Sun B, Lin J, Fu MW. Dependence of processing window and microstructural evolution on initial material state in direct electric resistance heat treatment of NiTi alloy. Mater Des 2018;139:549–64.

[58] Li Z, Xiao F, Chen H, Hou R, Cai X, Jin X. Atomic scale modeling of the coherent strain field surrounding Ni_4Ti_3 precipitate and its effects on thermally-induced martensitic transformation in a NiTi alloy. Acta Mater 2021;211:116883.

[59] Ke CB, Cao S, Zhang XP. Phase field modeling of Ni-concentration distribution behavior around Ni4Ti3 precipitates in NiTi alloys. Comput Mater Sci 2015;105:55–65.

[60] Michutta J, Somsen C, Yawny A, Dlouhy A, Eggeler G. Elementary martensitic transformation processes in Ni-rich NiTi single crystals with Ni_4Ti_3 precipitates. Acta Mater 2006;54(13):3525–42.

[61] Hamilton RF, Bimber BA, Palmer TA. Correlating microstructure and superelasticity of directed energy deposition additive manufactured Ni-rich NiTi alloys. J Alloys Compd 2018;739:712–22.

[62] Luo ZF, Liang YL, Long SL, Jiang Y, Wu ZL. Effects of ultra-refine grain and micro-nano twins on mechanical properties of 51CrV4 spring steel. Mater Sci Eng A 2017;690.

[63] Wu X, Cai C, Yang L, Liu W, Li W, Li M, et al. Enhanced mechanical properties of Ti-6Al-2Zr-1Mo-1V with ultrafine crystallites and nano-scale twins fabricated by selective laser melting. Mater Sci Eng A 2018;738:10–4.

[64] Li B, Wang L, Wang B, Li D, Oliveira JP, Cui R, et al. Tuning the microstructure, martensitic transformation and superelastic properties of EBF^3-fabricated NiTi shape memory alloy using interlayer remelting. Mater Des 2022;220:110886.

[65] Chen H, Xiao F, Liang X, Li Z, Li Z, Jin X, et al. Improvement of the stability of superelasticity and elastocaloric effect of a Ni-rich Ti-Ni alloy by precipitation and grain refinement. Scr Mater 2019;162:230–4.

[66] Wang X, Kustov S, Li K, Schryvers D, Verlinden B, Van Humbeeck J. Effect of nanoprecipitates on the transformation behavior and functional properties of a Ti–50.8at.% Ni alloy with micron-sized grains. Acta Mater 2015;82:224–33.